JGR Oceans

RESEARCH ARTICLE
10.1029/2019JC015165

Observations of Near-Bed Shear Stress in a Shallow, Wave- and Current-Driven Flow

Galen Egan[1], **Marianne Cowherd**[1], **Oliver Fringer**[1], **and Stephen Monismith**[1]

[1]Department of Civil and Environmental Engineering, Stanford University, Stanford, CA, USA

Key Points:
- Near-bed mean velocity profiles resemble canopy flow shear mixing layer profiles
- The addition of waves to mean currents increases the net drag felt by the flow
- Bed shear stresses estimated from standard techniques are poorly correlated to the measured bed shear stress

Correspondence to:
G. Egan,
gegan@stanford.edu

Citation:
Egan, G., Cowherd, M., Fringer, O., & Monismith, S. (2019). Observations of near-bed shear stress in a shallow, wave- and current-driven flow. *Journal of Geophysical Research: Oceans*, *124*, 6323–6344. https://doi.org/10.1029/2019JC015165

Received 20 MAR 2019
Accepted 11 AUG 2019
Accepted article online 15 AUG 2019
Published online 30 AUG 2019

Abstract We present in situ observations of mean and turbulent bottom stresses in a shallow, wave- and current-driven flow over a cohesive sediment bed on the eastern shoals of South San Francisco Bay. Data from a Nortek Vectrino Profiler deployed with its measurement volume overlapping the bed allowed us to calculate mean velocity profiles and turbulent Reynolds stresses over a 1.5-cm profile with 1-mm vertical resolution. Additional acoustic instrumentation and pressure sensors provided mean current and wave data. From these observations we found that biological roughness elements protruding from the sediment bed result in a mean velocity profile qualitatively similar to that found in canopy shear mixing layers. Despite fundamental differences between this measured velocity structure and that assumed by wave-current boundary layer models, we also found that the addition of waves to mean currents increases the net drag felt by the flow. The near-bed momentum flux was often dominated by a wave-induced component, which was generated by interactions between the wavy flow and the rough bed. Finally, we estimated the friction velocity using several different calculation methods and compared results to the measured bottom stress. This analysis revealed that traditional methods (e.g., log law fitting and point turbulence measurements) are consistent with one another when measuring the stress outside the wave boundary layer but were all poor approximations of the total stress at the bed.

Plain Language Summary We conducted field work in South San Francisco Bay to investigate how waves and tidal currents exert stress on a muddy sediment bed. Our data show that the average velocity near the bed is qualitatively similar to flow over a submerged canopy, for example, flow over seagrass, or atmospheric flow over a city. This velocity structure was caused by dense colonies of bottom-dwelling worms at the bed. We also found that the addition of waves to the tidal currents caused the flow to feel additional drag. Finally, we compared various methods of estimating the shear stress near the bed and found that none of the estimation methods could adequately represent the measured bed stress. These results are important for sediment transport modeling in estuaries.

1. Introduction

In a wide range of environmental flows, the shear stress induced by the bottom boundary is the most important quantity to estimate. The bottom stress generally sets both the mean velocity profile and turbulence production. It is also responsible for eroding sediment from the bed and mixing the sediment, momentum, and other scalars throughout the water column. Historically, it has been difficult to measure the near-bed vertical velocity gradient and turbulence statistics due to the millimeter-scale thickness of the bottom boundary layer (Nielsen, 1992). Therefore, the bottom stress is often parameterized based on a simplification of the time-averaged momentum equation in the horizontal (Schlichting & Gersten, 2016). Assuming x is aligned with the dominant flow direction, the 2-D time-averaged momentum equation is given by

$$\frac{\partial}{\partial z}(\overline{uw}) = -\frac{\partial \overline{p}}{\partial x} + \nu \frac{\partial^2 \overline{u}}{\partial z^2}, \tag{1}$$

where time-averaging is denoted by an overbar, and we have assumed that the time-averaged flow is steady and horizontally homogeneous; that is, $\overline{u}$ varies only in the vertical, z. The mean pressure gradient, $\frac{\partial \overline{p}}{\partial x}$, drives flow in its primary direction, x.

Specific derivations of bottom shear stress estimates arising from equation (1) will be reserved for section 3.2, but in general, there are inherent uncertainties in this approach. First and foremost, bottom boundary geometry is generally unknown without a field survey. Therefore, it is often assumed that the near-bed flow is

accurately described by flat plate boundary layer theory and the associated "law of the wall" (Schlichting & Gersten, 2016), which results in a viscous sublayer near the bed and a logarithmic layer above that. This is a reasonable assumption, as most geophysical flows follow the law of the wall (Grant & Madsen, 1986).

Despite its widespread use, flat plate boundary layer theory is not universally applicable. If the roughness elements at the bed are sufficiently large, the near-bed flow is better described by canopy flow theory, which predicts a thicker "shear mixing layer," rather than a viscous sublayer, beneath a modified logarithmic layer (Raupach et al., 1996). Canopy flow theory is applied to situations such as flow over seagrass beds (Ghisalberti & Nepf, 2002) or atmospheric flow over rough topography (Finnigan, 2000).

The addition of surface gravity waves to the mean flow can lead to further complications by altering near-bed momentum exchange dynamics. Specifically, waves provide a mean momentum flux in the positive (wave-traveling) direction, which can generate a mean flow in the wave boundary layer (Longuet-Higgins, 1953). These effects have been shown experimentally and in the field over seagrass canopies (Luhar et al., 2010, 2013). Waves can also modify the bottom stress and increase dissipation of turbulence kinetic energy (TKE) over a rough bed (Grant & Madsen, 1979). Bed roughness in the presence of waves is often quantified with the relative roughness A/k_b (Jonsson, 1966), where $A = u_b/\omega$ is the wave semiexcursion length, k_b is the Nikuradse roughness length, u_b is the bottom wave orbital velocity, and ω is the radian wave frequency. Typical values of A/k_b in San Francisco Bay are $\mathcal{O}(1-10)$ (Lacy & MacVean, 2016). Experimental work over rippled, noncohesive beds has found $A/k_b = \mathcal{O}(1-100)$ (Grant & Madsen, 1982), and in general, we would expect $A/k_b \gg 1$ for long period waves over a smooth bed.

Numerous models to describe the combined wave-current bed shear stress have been proposed over the years, and many imply that wave-current interactions increase the "apparent" bottom roughness and induce additional drag on the flow (Grant & Madsen, 1979; Styles et al., 2017; Styles & Glenn, 2000; You et al., 1991). However, one recent numerical study suggests that the opposite effect may be seen in estuarine environments with smooth beds; that is, the drag decreases with the addition of laminar waves (Nelson & Fringer, 2018).

Due to measurement constraints, we have been unable to verify whether the primary assumptions in most wave-current boundary layer models, specifically the assumption of a logarithmic velocity profile both within and outside the wave boundary layer and the assumption of applicability over a wide range of A/k_b, are valid in most estuarine systems. These uncertainties represent a significant knowledge gap for sediment transport modeling. Erosion of sediment from the bed is generally parameterized as a function of the bed shear stress (Mehta & Partheniades, 1982; Sanford, 2008; Sanford & Maa, 2001), which itself is parameterized based on flow statistics such as the mean velocity and wave conditions (Grant & Madsen, 1979).

Here, we use novel acoustic instrumentation to measure both mean and turbulent stresses within the bottom boundary layer in a shallow, wave- and current-driven flow over a cohesive sediment bed for a full spring-neap cycle. These results are compared with more traditional methods of estimating the bottom stress. Results are also analyzed in the context of wave-current boundary layer models to examine their validity in describing the bottom stresses found in wave- and current-driven flows.

2. Field Experiment

As part of a study examining cohesive sediment transport and flocculation dynamics, we deployed four instrument platforms on the shallow, eastern shoals of South San Francisco Bay from 17 July 2018 to 15 August 2018. This paper will focus on data collected at one of the platforms, as shown in Figure 1, which contained the bulk of our hydrodynamics instrumentation. At the platform, we deployed three acoustic Doppler velocimeters (ADVs) with their measurement volumes at 5, 15 and 45 cm above the bed (cmab), respectively. The ADVs sampled the pressure and 3-D velocity at 8 Hz for 14 min each hour.

The platform also held a Nortek Vectrino Profiler (Vectrino) placed with its measurement volume overlapping the bed, sampling at 64 Hz for 12 min each hour. The Vectrino measures all velocity components in 30 bins spaced at 1-mm intervals. A diver adjusted its vertical position in the water column until 10 bins were below the bed, and the remaining 20 bins were directly above it. It was positioned in this manner because the region of highest signal-to-noise ratio (SNR) is located 5 cm from the Vectrino transducer (Thomas et al., 2017). Thus, we obtained more reliable velocity profiles and turbulence statistics by ensuring that this region was at the bed. After deployment, the platform sank approximately 0.5 cm into the mud, so our profiles

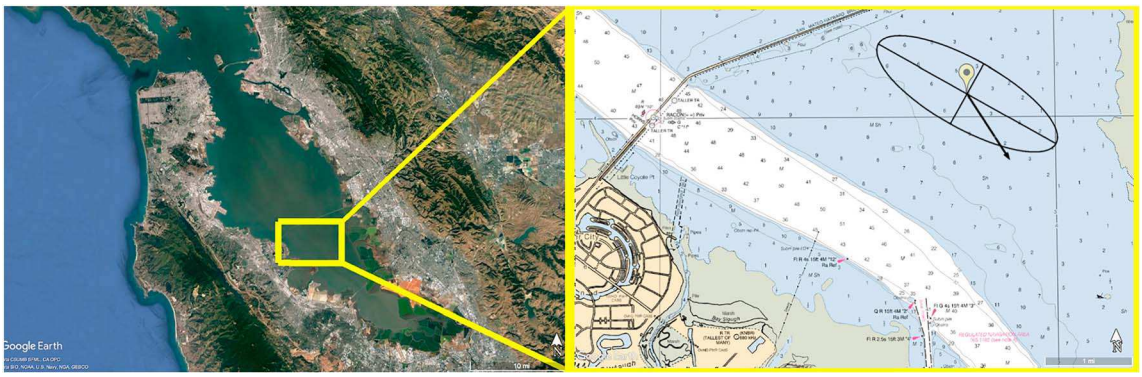

Figure 1. Deployment site in South San Francisco Bay. The platform was placed at approximately 1.5 m mean lower low water level on the shoals east of the main channel and south of the San Mateo Bridge. The major and minor components of the mean currents are depicted by the major and minor axes of the tidal ellipse centered at the platform, with the mean wind direction indicated by the arrow which corresponds to a fetch of approximately 28 km.

generally ranged from 0 to 1.5 cmab. Because the Vectrino does not have an onboard data logger, it was controlled by a custom data logger designed and fabricated by the Sexton Corporation.

We also deployed an RBRduo Bottom Pressure Recorder (BPR) sampling continuously at 6 Hz and an upward facing Nortek Aquadopp Acoustic Doppler Current Profiler (ADCP) to report mean current profiles over 0.1-m bins every 3 min based on 72 s of sampling. Table 1 summarizes the study site information (mean lower low water level [MLLW] and GPS coordinates), instrumentation, and measurement heights in centimeters above the bed.

3. Methods

3.1. Data Processing

Spikes were removed from ADV and Vectrino velocity time series using a phase-space despiking algorithm (Goring & Nikora, 2002). The velocity data were then rotated into the direction of maximum variance, that is, the first principal component calculated from the ADCP velocity time series. As seen in Figure 1, the major component was aligned in the along-channel direction and the minor component was aligned in the cross-channel direction. All u velocities reported herein are defined as the major component, and v velocities are the minor component. Vectrino and ADV data were rotated into the ADCP-derived principal directions for each of their respective burst periods, and all statistics were calculated with respect to the new directions; that is, the flow was considered statistically stationary during the burst period. For simplicity, we will focus our analysis on the major velocity component, which was on average 2.6 times larger in magnitude than the minor component.

During data processing, we noticed time-averaged negative vertical velocities in the ADV and Vectrino data, with magnitudes on the order of 0.5–1 cm/s. It is unlikely that this trend was due to particle settling. Simultaneous particle size distribution measurements collected with a Sequoia Scientific LISST-100x found a median particle size of $d_{50} = 72\mu m$ averaged over the deployment period. We also collected sediment cores at the study site and measured a bulk sediment density $\rho_s = 1,300$ kg/m^3 (Håkanson & Jansson, 2002). Assuming Stokes settling, this results in a settling velocity of 0.9 mm/s, significantly smaller than

Table 1
Instrument Platform Details

Location	MLLW (m)	Instruments	cmab
37.58745°N, 122.18530°W	1.5	Vectrino Profiler	0–1.5
		ADV	5, 15, 45
		ADCP	15–400
		BPR	100

Note. MLLW = mean lower low water level; ADV = acoustic Doppler velocimeter; cmab = centimeters above the bed; ADCP = acoustic Doppler current profiler; BPR = bottom pressure recorder.

the mean vertical velocities measured by the instruments. Therefore, we can likely attribute the mean vertical velocity to acoustic streaming, which is a mean flow induced by the instrument pressure transducer (Poindexter et al., 2011). To account for this, we detrended the vertical velocities over each burst period and will denote the resulting fluctuating velocities w.

After these quality control steps, the Reynolds stress tensor was calculated for each ADV burst based on the Benilov wave-turbulence decomposition (Benilov & Filyushkin, 1970). This method was not viable for the Vectrino, because unlike the ADV, it does not simultaneously log pressure. Therefore, the Reynolds stress tensor was calculated using the phase method (Bricker & Monismith, 2007). As a validation, the phase method was applied to the ADV data, with results matching those calculated from the Benilov method. The Vectrino Reynolds stress was further corrected using an algorithm that accounts for probe geometry and inherent variations in SNR over the profile (Thomas et al., 2017).

The Vectrino data were also used to estimate the TKE dissipation rate, which we calculated using a modified version of a spectral curve fitting method (Feddersen et al., 2007). Briefly, it involves curve fitting the high-frequency power spectrum in the inertial range, which we found in our data ranged from 3 to 8 Hz, with a noise floor correction based on the power spectral density between 20 and 30Hz. The near-bed TKE dissipation rate reached a maximum of $\epsilon = 1.5 \times 10^{-3}$ m^2/s^3 over the deployment period and was often orders of magnitude smaller. Using this value to estimate a Kolmogorov time scale results in $(\nu/\epsilon)^{1/2} = 0.026$ s. Therefore, the 64-Hz Vectrino sampling rate sufficiently resolved the turbulence spectrum for the vast majority of our stress estimates.

ADCP velocity data were smoothed with a 2-D median filter using a 3×9 kernel, that is, three vertical bins in space (0.3 m) and nine profiles in time (27 min). Profiles were then trimmed vertically to remove bins near the free surface. BPR pressure data were separated into 12-min bins such that one bin overlapped exactly with the Vectrino data each hour. We calculated spectra for each burst using the Welch method (Welch, 1967). On day 16 of the 28-day deployment, a large erosion event displaced the bed downward. Though we have no reason to believe that this changed the fundamental bed characteristics or the near-bed mean velocity structure, the region of highest SNR in the Vectrino profile was no longer aligned with the bed, leading to erroneous near-bed turbulence statistics and velocity gradients. Therefore, we restrict our analysis to the date range 17 July 2018 to 2 August 2018.

3.2. Wave-Current Interactions and Momentum Exchange

One of the primary goals of this study is to examine how the addition of surface waves to the mean flow modifies near-bed shear stress and momentum exchange dynamics. A time-averaging procedure (such as Reynolds averaging) will filter out the effects of waves in the mean velocity profile throughout most of the water column, but within the wave boundary layer the waves and currents interact nonlinearly to produce a shear stress that cannot be described by a linear superposition of the two individual stresses. Most wave-current boundary layer models imply that currents feel a rougher bottom in the presence of waves. This effect can be described through a relative increase in the drag coefficient,

$$C_D = \left(\frac{u_*}{u_r}\right)^2, \tag{2}$$

as waves are added to the mean flow. This definition follows from the quadratic drag law, $\tau_b = C_D u_r^2 = u_*^2$. Here, τ_b is the total bed shear stress, u_* is the friction velocity, and u_r is a reference velocity at height $z = z_r$, which we chose as $z_r = 1.2$ cmab. The choice of reference velocity is arbitrary as long as it is within the log layer rather than the wave boundary layer. For our data, the wave boundary layer never exceeded a thickness of 2 mm, so 1.2 cm was always sufficiently far from the boundary and well within the logarithmic velocity region.

To quantify the effects of waves on C_D, we calculated the wave Reynolds number

$$Re_\delta = \frac{u_b(2\nu/\omega)^{1/2}}{\nu}, \tag{3}$$

where ω is derived from the Vectrino horizontal velocity power spectrum and $(2\nu/\omega)^{1/2}$ is the Stokes boundary layer thickness. The wave-orbital velocity, u_b, was calculated by first subtracting the Vectrino burst-averaged velocity from its instantaneous velocity with

$$u_w(z) = u(z) - \overline{u}(z), \tag{4}$$

where the overbar denotes a time average over the burst period and u_w is the instantaneous perturbation velocity that includes effects of both waves and turbulence. Next, the root-mean-square of u_w averaged over the top five bins of the Vectrino profile was taken as a representative bottom orbital velocity,

$$u_b = \frac{1}{5}\sum_{j=1}^{5}\left(\overline{u_w(z_j)^2}\right)^{1/2}. \tag{5}$$

The physical mechanism through which waves affect the mean bottom stress is by modifying near-bed momentum exchange. Specifically, if the velocity is decomposed to include a mean, wave, and turbulence component,

$$u = \overline{u} + \tilde{u} + u', \tag{6}$$

where $\overline{u}$ is the mean (time-averaged) velocity, $\tilde{u}$ is the wave velocity, and u' is the fluctuating turbulence velocity, then the momentum flux (assuming that $\overline{w} = 0$) becomes

$$\overline{uw} = \overline{u'w'} + \overline{\tilde{u}w'} + \overline{u'\tilde{w}} + \overline{\tilde{u}\tilde{w}}. \tag{7}$$

By definition, waves and turbulence are uncorrelated when they coexist (Jiang & Street, 1991; Thais & Magnaudet, 1995) so the second and third terms on the right-hand-side of equation (7) are zero. For the case of irrotational, periodic waves, the last term on the right-hand side is also zero (Dean & Dalrymple, 1991), because the $\tilde{u}$ and $\tilde{w}$ components of the wave velocity are 90° out of phase with one another, leaving only the turbulent Reynolds stress $\overline{u'w'}$. However, the assumption of irrotationality is not always valid, especially near boundaries, for example, the wind-driven surface layer or near the bed (Magnaudet & Masbernat, 1990). This implies that $\overline{\tilde{u}\tilde{w}}$, which we will call the wave momentum flux, can be nonnegligible, a situation that will be explored further in section 4.4.

3.3. Shear Stress Estimation Methods

Starting with the 2-D momentum balance (equation (1)), there are multiple ways to estimate the bottom shear stress, each relying on different assumptions and measurement devices. We can integrate equation (1) from an arbitrary depth, z, to the mean-free surface height, H, assuming that the horizontal pressure gradient is vertically uniform to obtain

$$(\overline{uw})_s - (\overline{uw})_z = -\frac{\partial \overline{p}}{\partial x}(H - z) + \left(\nu\frac{\partial \overline{u}}{\partial z}\right)_s - \left(\nu\frac{\partial \overline{u}}{\partial z}\right)_z. \tag{8}$$

Here, a subscript s denotes a surface value, and a subscript z denotes a value at arbitrary height z. Next, we define the total shear stresses at the surface and height z as τ_s and $\tau_T(z)$, respectively,

$$\tau_s = \left(\nu\frac{\partial \overline{u}}{\partial z}\right)_s - (\overline{uw})_s, \quad \tau_T(z) = \left(\nu\frac{\partial \overline{u}}{\partial z}\right)_z - (\overline{uw})_z. \tag{9}$$

This implies that the shear stress has both a viscous component and a component due to the vertical momentum flux. This also allows us to write equation (8) as

$$-\tau_s + \tau_T(z) = -\frac{\partial \overline{p}}{\partial x}(H - z). \tag{10}$$

Assuming that the stress is negligible at the free surface and defining the bottom stress in terms of a friction velocity, $\tau_T(z = 0) = u_*^2$, we obtain

$$u_*^2 = -H\frac{\partial \overline{p}}{\partial x}, \tag{11}$$

where we retain the convention that a negative pressure gradient drives flow in the positive x direction. This results in an estimation method for u_* based on measuring the driving pressure gradient. Though we tried to estimate u_* in this manner, results were highly inconsistent with other estimation methods because it relied on publicly available tide gage data rather than our own instruments. Therefore, we will not report those estimates here. Substitution of equation (11) into equation (10) results in the profile of shear stress throughout the water column,

$$\tau_T(z) = u_*^2\left(1 - \frac{z}{H}\right). \tag{12}$$

Within the viscous sublayer, which we define as $z < \delta_v$, where δ_v is the viscous sublayer thickness, only the viscous component of the shear stress is significant, that is, $\tau_T(z) \approx \left(\nu \frac{\partial \overline{u}}{\partial z}\right)_z$, resulting in the viscous sublayer velocity profile,

$$\overline{u} = \frac{u_*^2 z}{\nu}. \tag{13}$$

Therefore, the near-bed mean velocity gradient can be used to estimate the friction velocity with

$$u_* = \left(\nu \frac{\partial \overline{u}}{\partial z}\right)^{1/2}. \tag{14}$$

This method has only recently become possible in situ due to advances in ADV technology like the Vectrino Profiler used in this study. We will apply equation (14) to our Vectrino mean velocity data as one method for estimating the bed shear stress. Further from the boundary, the viscous component of the stress becomes negligible, leaving the shear stress equal to the momentum flux at arbitrary height z, that is, $\tau_T(z) = -(\overline{uw})_z$, leading to

$$-(\overline{uw})_z = u_*^2 \left(1 - \frac{z}{H}\right). \tag{15}$$

Rearranging, we obtain another estimate for the friction velocity,

$$u_* = |\overline{uw}|_z^{1/2} \left(1 - \frac{z}{H}\right)^{-1/2}. \tag{16}$$

Because this estimate is based on the full momentum flux, $\overline{uw}$, it would include the effects of the wave-induced momentum flux in a combined wave-current flow. If instead we set $\tau_T(z) = -(\overline{u'w'})_z$, that is, the phase or Benilov method decomposed turbulent Reynolds stress at height z, then we obtain

$$u_* = |\overline{u'w'}|_z^{1/2} \left(1 - \frac{z}{H}\right)^{-1/2}. \tag{17}$$

This estimate of the bottom stress is based solely on the turbulence statistics and has been widely used in estuarine boundary layer studies (MacVean & Lacy, 2014; Stacey et al., 1999; Stacey & Ralston, 2005). Including the factor of $\left(1 - \frac{z}{H}\right)^{-1/2}$ in each of the above estimates (equations (16) and (17)) ensures that we take into account the linear decrease of the momentum flux with height z from the bed, as assumed in turbulent open channel flow theory. This indicates that as long as the surface shear stress is negligible and the total shear stress follows its assumed linear profile (equation (12)), u_* can be estimated by measuring the momentum flux anywhere in the water column. This is significant because $\overline{uw}$ can be easily measured with a single high-frequency velocimeter. In this paper, we will apply equation (17) to ADV data to estimate the bottom stress.

Retaining the assumption that $\tau_T(z) = -(\overline{u'w'})_z$, we can estimate the friction velocity yet another way following from the linear stress profile (equation (12)). Close to the bed, but not within the viscous sublayer, we can assume that $z/H \ll 1$, which reduces equation (12) to

$$-\overline{u'w'} = u_*^2. \tag{18}$$

Invoking Prandtl's mixing length hypothesis (Prandtl, 1925) leads to the logarithmic law of wall,

$$\overline{u}(z) = \frac{u_*}{\kappa} \ln\left(\frac{z}{z_0}\right), \tag{19}$$

where z_0 is the bottom roughness and κ is the von Kármán coefficient. Recent work has suggested that $\kappa = 0.38$ is the most appropriate value for a boundary layer flow (Nagib & Chauhan, 2008), but we chose a constant $\kappa = 0.41$ for consistency with previous studies in South San Francisco Bay (e.g., Bricker et al., 2005; Cheng et al., 1999). The mean velocity profile can be measured with a profiling current meter, and equation (19) can be fit for optimal values of u_* and z_0. This is another common way of estimating bottom

Table 2
Summary of Each Method Used to Estimate the Friction Velocity

Instrument	cmab	Method	Variable
Vectrino	≈ 0.5	Viscous stress + momentum flux (equation (22))	$\left\lvert \nu\frac{\partial\overline{u}}{\partial z} - \overline{uw}\right\rvert_b^{1/2}$
Vectrino	≈ 0.5	Viscous + turbulent stress (equation (23))	$\left\lvert \nu\frac{\partial\overline{u}}{\partial z} - \overline{u'w'}\right\rvert_b^{1/2}$
Vectrino	≈ 0.5	Reynolds stress (equation (24))	$\left\lvert \overline{u'w'}\right\rvert_b^{1/2}$
Vectrino	0.6–1.5	Log law fit (equation (19))	u_*
Vectrino	0.6–1.5	Canopy log law fit (equation (20))	u_{*_c}
Vectrino	0.4–0.6	Viscous sublayer fit (equation (13))	$\left\lvert \nu\frac{\partial\overline{u}}{\partial z}\right\rvert^{1/2}$
ADV	5	Reynolds stress (equation (17))	$\left\lvert \overline{u'w'}\right\rvert_5^{1/2}\left(1-\frac{5}{H}\right)^{-1/2}$
ADCP	20–100	Canopy log law fit (equation (20))	u_{*_A}

Note. cmab = centimeters above the bed; ADV = acoustic Doppler velocimeter; ADCP = acoustic Doppler current profiler.

friction in estuarine flows (Cheng et al., 1999) and can be applied to both the Vectrino and ADCP mean velocity profiles.

If the bottom boundary is better represented by a canopy than a flat plate (which was the case for our data), the log law (equation (19)) is modified to become

$$\overline{u}(z) = \frac{u_{*c}}{\kappa}\ln\left(\frac{z-d}{z_0}\right). \tag{20}$$

Here, u_{*_c} is the canopy friction velocity, and d denotes the canopy displacement height, which is given by

$$\frac{d}{h} = 1 - \frac{0.1}{C_{\mathrm{DC}}ah}, \tag{21}$$

where h is the physical canopy height, C_{DC} is the canopy drag coefficient, and a (m^{-1}) is the canopy density (Nepf, 2012). Ideally, C_{DC} and a are estimated from canopy geometry. However, we did not have this information when we fit equation (20) to mean velocity profiles, so we regressed for d in addition to u_{*_c} and z_0.

Given the number of options available for estimating u_*, it is necessary to define a "true" bottom stress against which we can compare the different estimation methods. For this, we chose the sum of the viscous stress and momentum flux (the total shear stress τ_T in equation (9)) measured in the Vectrino bin 1 mm, or one measurement bin, above the top of the canopy roughness elements, that is,

$$u_* = \left\lvert \nu\frac{\partial\overline{u}}{\partial z} - \overline{uw}\right\rvert_b^{1/2}, \tag{22}$$

where the subscript b denotes a bottom measurement. The canopy height was defined as the kink point in the velocity profile below which the mean velocity was approximately zero (e.g., $h = 3.9$ mm in Figure 3). This was computed as the measurement bin 2 mm below the location of the maximum vertical velocity gradient and confirmed through visual inspection of each velocity profile. Though the canopy height varied over the deployment period, equation (22) was usually applied at 0.5 cmab.

If we remove the wave momentum flux from the total momentum flux in equation (22), we obtain an estimate of the friction velocity due solely to the currents,

$$u_* = \left\lvert \nu\frac{\partial\overline{u}}{\partial z} - \overline{u'w'}\right\rvert_b^{1/2}. \tag{23}$$

We can also ignore the viscous component in equation (23) and estimate the friction velocity based on the measured turbulent stress near the bed,

$$u_* = \left\lvert \overline{u'w'}\right\rvert_b^{1/2}. \tag{24}$$

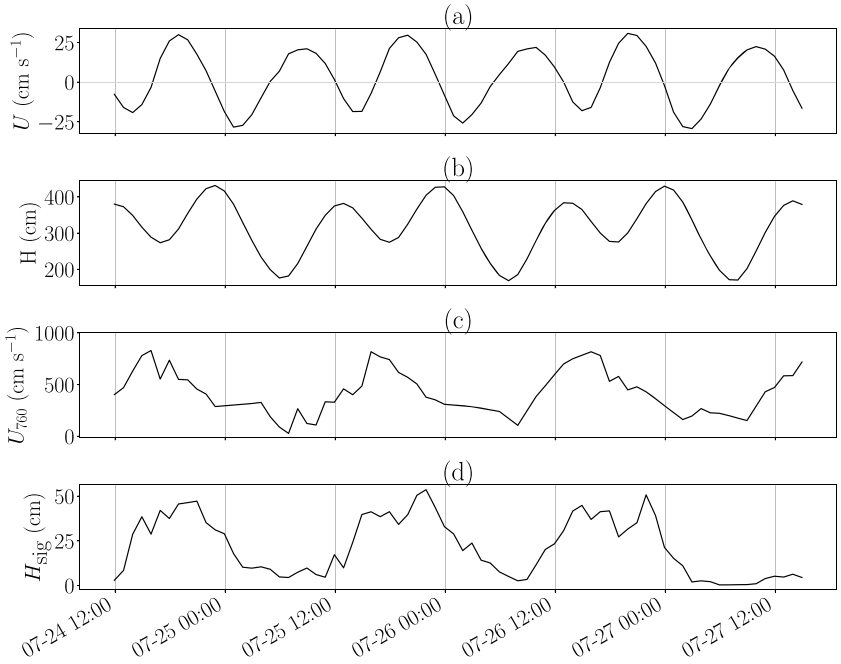

Figure 2. (a) Depth-averaged velocity measured by the ADCP, (b) total water depth measured by the BPR, (c) wind velocity at 760 cm above mean sea level measured at the Redwood City National Oceanic and Atmospheric Administration National Data Buoy Center station, and (d) significant wave height calculated from bottom pressure recorder-derived power spectra during three days of our deployment.

All of the u_* estimation methods that we use in this paper are summarized in Table 2, which lists the instrument used for measurement, the height above the bed at which the measurement was taken, the method, and the given variable.

4. Results and Discussion

4.1. Site Conditions

Tidal currents ran primarily northwest-southeast (ebb and flood, respectively; see tidal ellipse in Figure 1), with maximum depth-averaged current (denoted U) magnitudes ranging from 20 to 30 cm/s (Figure 2a). The mean tidal range was approximately 2 m, as seen by the total water depth, D, in Figure 2b. Data taken from the National Oceanic and Atmospheric Administration National Data Buoy Center Redwood City weather station approximately 10 km west of the study site showed diurnal northwesterly winds that gained strength in the early afternoon and lasted until evening, with maximum wind speeds of approximately 10 m/s (see Figure 1 for primary direction and fetch and Figure 2c for wind velocity at 7.6 m above mean sea level). The wind drove primarily westerly waves that increased in height each afternoon as shown by the significant wave height, H_{sig}, in Figure 2d. Spectral analysis of the wave signal showed peak frequencies ranging from 0.2 to 0.5 Hz.

4.2. Mean Boundary Layer Characteristics

In Figure 3a, we show a characteristic velocity profile measured by the Vectrino, time-averaged over a single 12-min burst period. The profile has three distinct regions; from 0 to 3 mm above the bed, the mean velocity is approximately zero. This is likely due to the abundance of biological material (mostly feeding tubes built by *Sabaco elongatus*, a benthic worm species) protruding from the bed, which were found on the surface of sediment cores collected at the study site (see Figure 4). From 3 to 6 mm above the bed, the velocity increases approximately linearly in height. This is suggestive of the viscous sublayer described in equation (13). Above this region the flow transitions to a logarithmic profile, which could be described by either the standard log law (equation (19)) or given the benthic worm canopy, the canopy log law (equation (20)).

In a theoretical log layer, the friction velocities based on the viscous sublayer (equation (13)) and the log law (equation (19)) will match because the near-bed velocity gradient sets the friction velocity higher in the water column. To check this, we fit equation (19) to the upper (logarithmic) part of the velocity profile

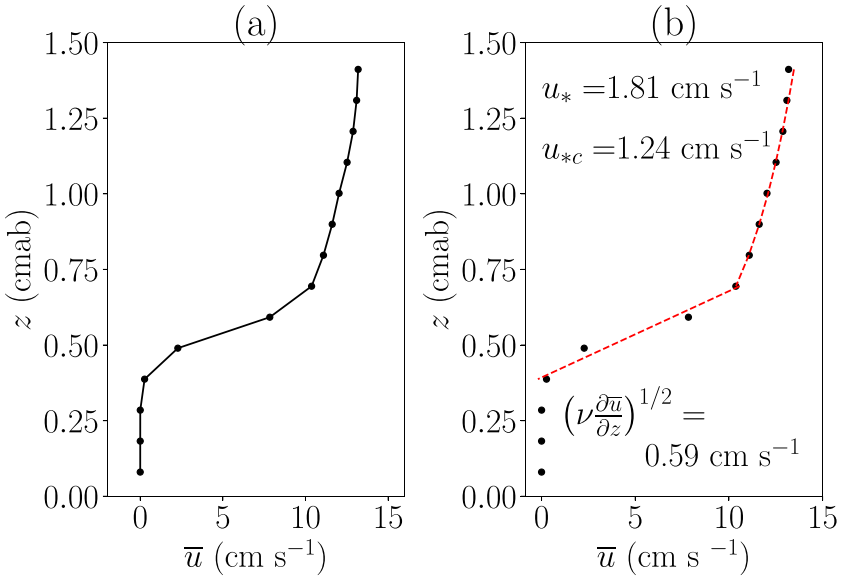

Figure 3. Vectrino burst-averaged profiles of (a) velocity, with (b) showing fits (dashed red lines) of the viscous sublayer velocity profile (equation (13), $r^2 = 0.93$), the standard log law fit for u_* (equation (19), $r^2 = 0.99$), and the canopy log law fit for u_{*_c} (equation (20), $r^2 = 0.99$, fit not shown because it overlaps with the standard log law) to the mean velocity profile.

and equation (13) to the lower (linear) part of the velocity profile as seen by the dashed lines in Figure 3b. However, this fitting procedure showed that u_* is over 3 times larger in the log layer compared to the linear region. This trend was consistent throughout the measurement period, indicating that the law of the wall is not strictly applicable for this system despite looking qualitatively correct. Furthermore, classic scaling for the viscous sublayer dictates that its dimensional thickness is given by $\delta_\nu = \frac{5\nu}{u_*}$. Using $u_* = \left(\nu\frac{\partial\overline{u}}{\partial z}\right)^{1/2}$ from Figure 3b, this corresponds to a thickness of $\delta_\nu \approx 0.8$ mm; using u_* from the fit to equation (19), we obtain a thickness of $\delta_\nu \approx 0.2$ mm. Both of these values are much smaller than the $\delta_\nu \approx 3$-mm thickness seen in Figure 3. Fitting the canopy log law (equation (20)) to the logarithmic portion of the velocity profile produces a u_{*_c} value that is closer to $\left(\nu\frac{\partial\overline{u}}{\partial z}\right)^{1/2}$ but still larger by a factor of 2.

Some of the discrepancy between the near-bed gradient and log law estimates of u_* could be explained by the increased fluid viscosity induced by high concentrations of suspended sediment near the bed. However, suspended sediment concentrations estimated from Vectrino acoustic backscatter calibration were $\mathcal{O}(1-10)$ g/L in the linear velocity region (not shown); previous studies have demonstrated that significant kinematic viscosity changes would not be expected for this range of concentrations (Gust, 1976). However, sediment-induced stratification could affect turbulence dynamics in this region and will be explored in a forthcoming paper.

Another explanation for the friction velocity estimation discrepancy can be found in the section of the velocity profile closest to the bed. Including this region of near-zero velocity, the profile looks similar to a canopy

Figure 4. Sediment core recovered from the study site showing a canopy composed of *Sabaco elongatus* worm tubes. The numbers on the ruler indicate centimeters above the bottom of the core.

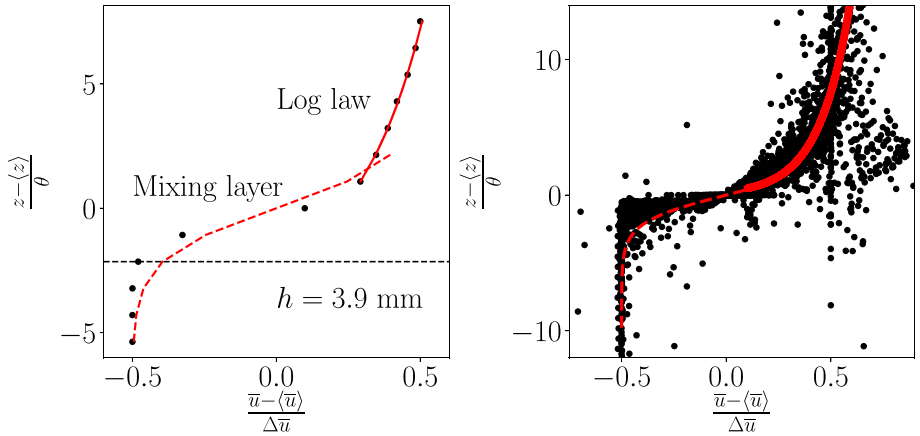

Figure 5. (a) The mean velocity profile shown in Figure 3, with the dashed red line denoting the fit to equation (25) ($r^2 = 0.96$), the solid red line denoting the fit to equation (20) ($r^2 = 0.99$), and the dashed black line indicating the canopy height at $h = 3.9$ mm and (b) velocity profiles from the entire study period overlaid on one another, with the same fits as in (a). For (b), we used a nonlinear least squares fitting procedure to determine optimal values of θ, $\langle\overline{u}\rangle$, $\langle z\rangle$, u_*, and z_0.

flow shear mixing layer over submerged vegetation (Ghisalberti & Nepf, 2002). To test the applicability of a canopy flow model to these velocity profiles, we fit them to the hyperbolic tangent profile

$$\frac{\overline{u} - \langle\overline{u}\rangle}{\Delta\overline{u}} = 0.5 \tanh\left(\frac{z - \langle z\rangle}{2\theta}\right), \tag{25}$$

where $\Delta\overline{u} = \overline{u}_2 - \overline{u}_1$ and $\langle\overline{u}\rangle = 0.5(\overline{u}_1 + \overline{u}_2)$. Here, $\overline{u}_1$ is the minimum velocity over the profile, $\overline{u}_2$ is the maximum velocity, $\langle z\rangle$ is the height corresponding to $\langle\overline{u}\rangle$, and θ is the momentum thickness given by

$$\theta = \int_{-\infty}^{\infty}\left[\frac{1}{4} - \left(\frac{\overline{u} - \langle\overline{u}\rangle}{\Delta\overline{u}}\right)^2\right]\mathrm{d}z. \tag{26}$$

Figure 5a shows the fit to equation (25) using the same data as shown in Figure 3. This fit is expected to be qualitatively correct until approximately two canopy heights above the bed, where the canopy height, h, is the mean physical height of the canopy elements. Above $z = 2h$, the velocity profile follows the canopy log law (equation (20)) set by the mean pressure gradient (Ghisalberti & Nepf, 2002).

Using this corrected log law, the velocity profiles follow the expected canopy flow/shear mixing layer profile, with the fit to the hyperbolic tangent (equation (25)) matching best until approximately 8 mm above the bed (i.e., two canopy heights) and the fit to the canopy log law (equation (20)) matching best above that. Most importantly, this model captures the width of the linear portion of the velocity profile more accurately than the viscous sublayer scaling. Over the study period, the average roughness length estimated from the fitting procedure was $z_0 = 0.9$ mm, consistent with the length of worm tubes and other features shown in Figure 4. The roughness length increased during the wavy period each afternoon; these wave-current dynamics will be discussed further in section 4.3.

The canopy flow model is consistent throughout the study period. Figure 5b shows that despite some outliers, most of the measured velocity profiles collapse onto the expected functional form. This is a significant result because it shows that the fundamental velocity structure within 1 cm of the bed cannot be inferred from measurements outside that region. A log law fit to the mean velocity further from the bed generally implies a corresponding mean velocity gradient in the viscous sublayer. However, because the canopy induces a shear mixing layer rather than a viscous sublayer, the mean shear felt by the bed is substantially lower.

4.3. Wave-Mean Flow Interactions

Plotted in Figure 6 are three estimates of the drag coefficient calculated from equation (2), bin-averaged by the wave Reynolds number, Re_δ. When calculating C_D, we chose to estimate u_* with the canopy log law

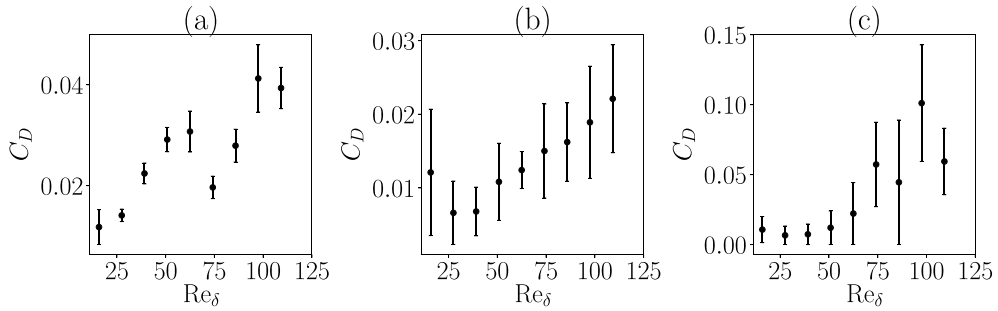

Figure 6. The drag coefficient $C_D = \left(\frac{u_*}{u_r}\right)^2$, bin averaged by wave Reynolds number. The friction velocity, u_*, was estimated using (a) the canopy log law (equation (20)), (b) the summation of the viscous and turbulent stresses 1 mm above the canopy top (equation (23)), and (c) the summation of the viscous stress and full momentum flux 1 mm above the canopy top (equation (22)). Error bars denote the standard error on the Re_δ bin averaging.

(equation (20)) for Figure 6a, with the summation of the viscous and turbulent stresses 1 mm above the canopy top (equation (23)) for Figure 6b, and with the full bottom stress, the summation of the viscous stress and full momentum flux 1 mm above the canopy top (equation (22)) in Figure 6c. The wave Reynolds number reached a maximum value of $Re_\delta \approx 125$ over the deployment period, which would indicate a laminar boundary layer for oscillatory flow over a smooth bed (Jensen et al., 1989). As discussed in the previous section, though, the bed was extremely rough, which can lead to turbulent behavior at far lower Re_δ (Chen et al., 2007).

In Figure 6a, despite an outlying decrease near $Re_\delta = 75$, the drag coefficient generally increases with Re_δ. This suggests that the mean flow feels greater drag in the presence of waves. Based on the definition of C_D (equation (2)), for a constant bed shear stress, the measured velocity at the reference height decreased with increasing wave strength. Using the log law (equation (19)), equation (2) can be equivalently expressed in terms of bottom roughness; that is, $C_D = \left(\frac{\kappa}{\ln(z_r/z_0)}\right)^2$ (Cheng et al., 1999). This explicitly shows that an increase in C_D corresponds to a larger apparent bottom roughness, a result that agrees qualitatively with most wave-current boundary layer models.

As discussed in the previous section, the near-bed flow structure is not adequately described by a logarithmic velocity profile, even when using the corrected canopy log law (equation (20)). Therefore, the stress in Figure 6b, defined as the sum of the viscous and turbulent stresses, may be more representative of the shear stress response to wave forcing. Here, the error bars are substantially larger; this additional scatter is due to the burst periods when $\overline{u'w'}$ and $\frac{\partial \bar{u}}{\partial z}$ were the same sign near the bed, resulting in a negative shear production term and complicating the relationship between the reference velocity, u_r, and the friction velocity, u_*, in equation (2). The relative occurrence of these negative production burst periods can be seen in Figure 10a in section 4.4. Regardless, the average drag coefficient tends to increase with increasing wave strength, supporting the assertion that waves increase bottom drag over a rough bed.

Finally, we can define C_D using the full bed stress, the sum of the viscous stress and full momentum flux (equation (23)). This is shown in Figure 6c and displays a similar trend to the previous two definitions. Error bars are again large, but the magnitude by which C_D increases over the range of Re_δ is also much larger (note the change in y axis scale). This is not surprising because this definition of u_* explicitly includes wave effects through the wave momentum flux, $\tilde{u}\tilde{w}$. Therefore, we would expect an increase in Re_δ (i.e., stronger waves) to result in a substantially larger C_D, because C_D is proportional to u_*^2.

We initially planned to use these data to test the applicability of various wave-current boundary layer models. However, many widely used models (Grant & Madsen, 1979; Styles et al., 2017; Styles & Glenn, 2000) assume that the mean velocity within the wave boundary layer follows a log law. For our data, the near-bed mean velocity is better described by canopy flow theory (equation (25)), which represents fundamentally different dynamics. Therefore, we restrict our analysis to affirming the qualitative result that wave-current interactions increase the apparent bottom roughness, without explicitly comparing different models to our data.

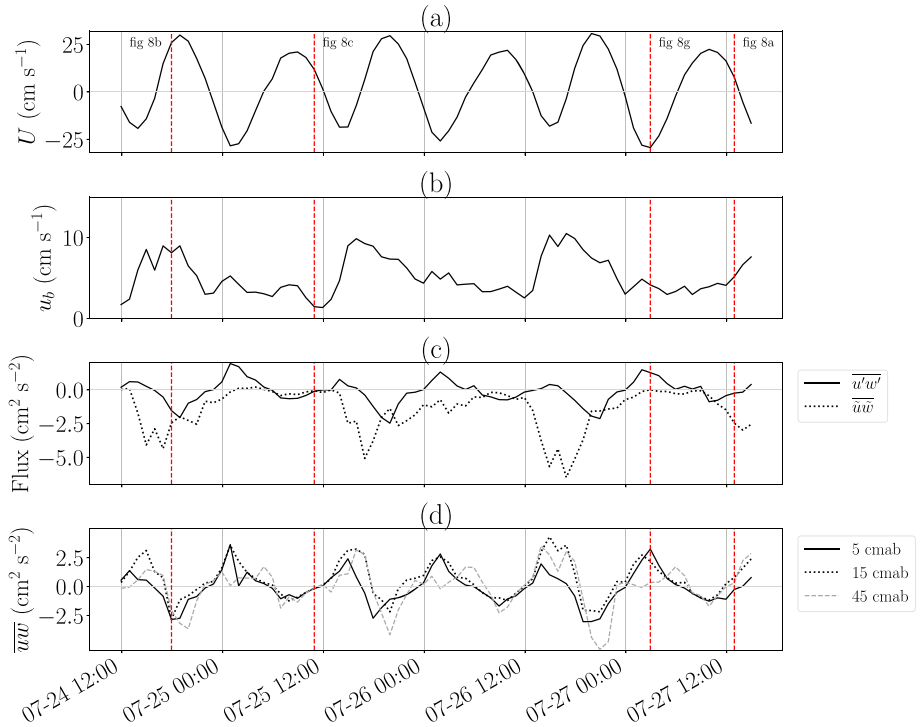

Figure 7. (a) Depth-averaged velocity, U, calculated from acoustic Doppler current profiler data, (b) bottom wave-orbital velocity calculated from Vectrino data, (c) Vectrino turbulent Reynolds stress ($\overline{u'w'}$) and wave momentum flux ($\overline{\tilde{u}\tilde{w}}$) at 0.6 cmab, and (d) acoustic Doppler velocimeter total vertical momentum flux ($\overline{uw}$), calculated during 3 days of the deployment corresponding to Figure 2, which also contains wind data for this time period. The red dashed vertical lines in each panel indicate the times corresponding to different panels in Figure 8.

4.4. Turbulent Boundary Layer Characteristics

Figure 7c shows the turbulent Reynolds stress and wave momentum flux, denoted by $\overline{u'w'}$ and $\overline{\tilde{u}\tilde{w}}$, respectively, calculated via the phase method from the Vectrino data during 3 days of the deployment corresponding to Figure 2. Because the Vectrino provides a profile of Reynolds stresses for each burst, the values plotted are taken from 0.6 cmab. We chose this point in the profile because it generally corresponded to the maximum magnitude wave momentum flux, displayed variations in the turbulent Reynolds stress of similar magnitude, and was also within the Vectrino region of highest SNR. Figure 7d shows the total vertical momentum flux, $\overline{uw}$, calculated from ADV data at three heights above the bed. For clarity, these values are not decomposed into their wave and turbulence components, but in general, we expect $\overline{uw} = \overline{u'w'} + \overline{\tilde{u}\tilde{w}}$. Figures 7a and 7b show the corresponding depth-averaged current, U, and bottom wave-orbital velocity, u_b, respectively.

The Reynolds stress, $\overline{u'w'}$, shown in Figure 7c, varies tidally. As expected, it is negative when the depth-averaged current is positive (during flood tides) and positive when the depth-averaged current is negative (during ebb tides). This ensures that the production term in the TKE equation, $-\overline{u'w'}\frac{\partial \bar{u}}{\partial z}$, is positive. Conversely, $\overline{\tilde{u}\tilde{w}}$ varies diurnally and is more negative with the onset of large afternoon wind waves. During periods of strong wave activity, $\overline{\tilde{u}\tilde{w}}$ can dominate $\overline{u'w'}$ by up to an order of magnitude in absolute value. When wave action decreases overnight and through the morning, $\overline{u'w'}$ and $\overline{\tilde{u}\tilde{w}}$ are generally of similar magnitude.

The ADV data in Figure 7d show similar trends, namely, a coherent tidal variation in momentum flux with a superimposed diurnal variation due to waves. These data also allow us to evaluate the applicability of the linear shear stress profile described by equation (15). For that equation to hold, we would expect the absolute value of the momentum flux to decrease with distance from the boundary. This is sometimes true, for example, each night near 00:00. But the clearest signal in this time series comes from the ADV at 45 cmab, which shows an increase in momentum flux magnitude each afternoon during the onset of strong wind waves. Interestingly, this increase is positive when the mean currents are negative (e.g., just after 26 July

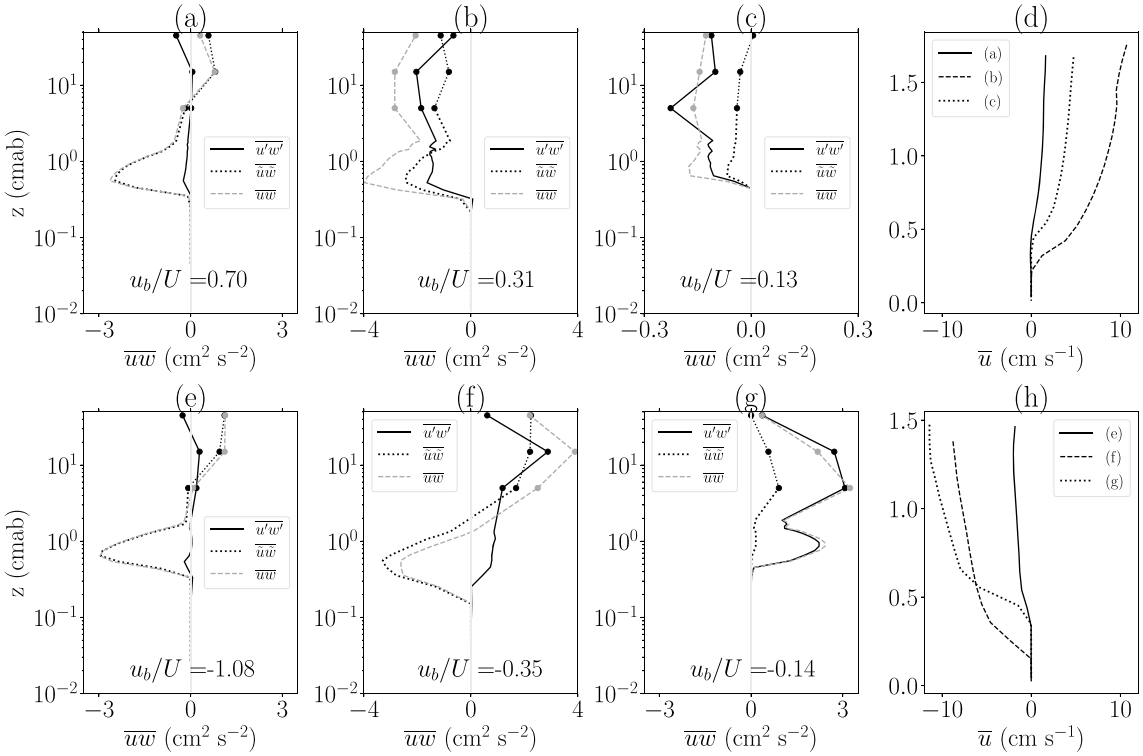

Figure 8. Turbulent Reynolds stress and wave momentum flux profiles (black solid and black dotted lines, respectively) and total momentum flux (gray dashed line) for (a) strong waves, positive mean shear; (b) moderate waves, positive mean shear; (c) weak waves, positive mean shear; (e) strong waves, negative mean shear; (f) moderate waves, negative mean shear; and (g) weak waves, negative mean shear. Panels (d) and (h) show the mean velocity profiles corresponding to each plot in the top and bottom rows, respectively, with the vertical axis showing distance above the bed in linear scale rather than log scale. The data closest to the bed (0–1.5 cmab) were taken with the Vectrino, while the three data points furthest from the bed (denoted with circular markers) were calculated using the acoustic Doppler velocimeters at 5, 15, and 45 cmab, respectively.

12:00) and negative when the mean currents are positive (e.g., later that afternoon), contrasting with the exclusively negative wave momentum fluxes measured by the Vectrino in Figure 7c.

To further probe the turbulence structure both within and outside the boundary layer, Figures 8a–8c show representative profiles of the turbulent Reynolds stress and wave momentum flux, along with the total momentum flux $\overline{uw}$, for varying magnitudes (strong, moderate, and weak) of the ratio $u_b/U > 0$. Figures 8e–8g show the same stresses for similar magnitudes of u_b/U but for $u_b/U < 0$. The boundaries between strong, moderate, and weak waves were set such that we had an equal number of burst periods in each category. Strong wave bursts were defined as $|u_b/U| > 0.40$, moderate wave bursts were defined as $0.21 < |u_b/U| < 0.40$, and weak wave bursts were defined as $|u_b/U| < 0.21$. A positive u_b/U indicates that the tide is flooding, that is, flowing toward the southeast (see tidal ellipse in Figure 1) and that the mean shear, $\frac{\partial \bar{u}}{\partial z}$, is positive. Because the waves almost always propagate toward the eastern shore, the waves and currents are generally additive in this case. Conversely, $u_b/U < 0$ indicates that the tide is ebbing, the mean shear is negative, and the waves and currents oppose each other.

When waves are strong and the mean shear is positive (Figure 8a), $\overline{u'w'}$ is relatively small over the measurement profile compared to $\overline{\tilde{u}\tilde{w}}$, which reaches a maximum magnitude near 0.6 cmab. Above that point, it decays to zero but becomes slightly positive at 15 and 45 cmab. When waves are strong but oppose the tides (Figure 8e), the profile displays almost identical behavior: a strong negative peak in $\overline{\tilde{u}\tilde{w}}$ near the bed and a similar weaker trend toward positive stresses at 15 and 45 cmab. In both cases, the current magnitude is relatively weak compared to the wave-induced velocities, so it is reasonable to infer that the sign change in the mean flow has a negligible effect. The positive stresses at 15 and 45 cmab, however, were not expected; we saw in Figure 7d that the wave-driven momentum flux was often positive when the currents were negative (this situation matches Figure 8e), but in Figure 8a the wave-driven momentum flux is positive when the current is also positive.

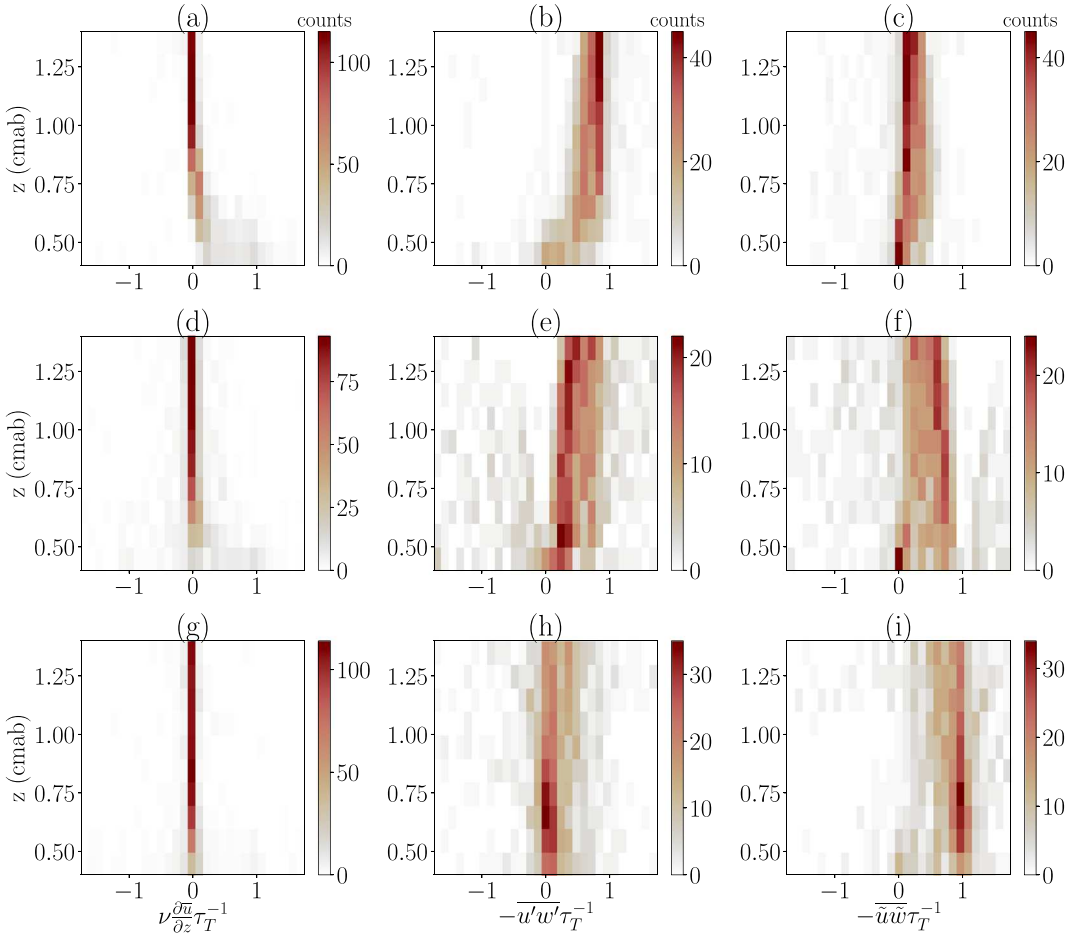

Figure 9. Histograms over 0.4–1.4 cmab from the Vectrino profile showing counts of the different components of the total stress for varying wave conditions: (a) viscous stress during weak wave bursts, (b) turbulent stress during weak wave bursts, (c) wave stress during weak wave bursts, (d) viscous stress during moderate wave bursts, (e) turbulent stress during moderate wave bursts, (f) wave stress during moderate wave bursts, (g) viscous stress during strong wave bursts, (h) turbulent stress during strong wave bursts, and (i) wave stress during strong wave bursts. The within-canopy portions of the profiles are neglected in each panel because the excessive near-zero counts skewed the color bar, making the rest of the profile difficult to interpret.

When the current magnitude increases relative to the wave-induced velocity, the turbulent Reynolds stress begins to make up an increasing proportion of the total stress, as shown in Figures 8b and 8f. The wave momentum flux is still strongly negative below 1 cmab in Figure 8b and remains slightly negative further from the bed. When the sign of the current changes (Figure 8f), the wave-induced stress at 45 cmab also changes sign; this behavior exactly matches the wavy periods in Figure 7d.

The case of relatively weak waves is shown in Figures 8c and 8g. It is only when the wave-induced velocity is much weaker than the current velocity that the turbulent Reynolds stress dominates the total stress profile. In Figure 8c, the Reynolds stress and wave momentum flux are both negative over the entire profile during the flood tide. Conversely, they are positive over the entire profile in Figure 8g during the ebb tide, providing further evidence that both the magnitude and direction of the total momentum flux and its components are determined by the interplay of waves and currents, rather than a simple superposition of each in absence of the other. In both the weak wave case and the moderate wave case, the total stress could be represented by a linear profile, as the stresses generally decay with distance from the bed. This would not be a reasonable assumption for the strong wave cases where the shear stress approaches larger values (in magnitude) away from the bed, perhaps due to wind stress at the surface.

The profiles in Figure 8 provide valuable snapshots of the stress both within and outside the boundary layer, but we can also show a more comprehensive momentum balance in the near-bed region for the entire

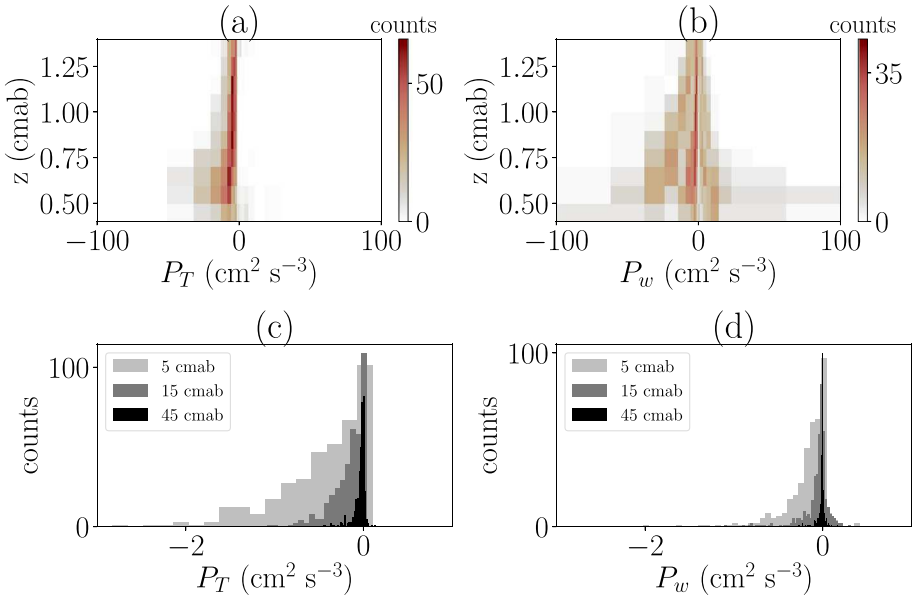

Figure 10. Histograms of (a) Vectrino turbulence kinetic energy production from 0.4 to 1.4 cmab; (b) Vectrino wave production from 0.4 to 1.4 cmab; (c) turbulence kinetic energy production from the ADV at 5 cmab (light gray), the ADV at 15 cmab (gray), and the ADV at 45 cmab (black); and (d) wave production from the ADV at 5 cmab (light gray), the ADV at 15 cmab (gray), and the ADV at 45 cmab (black). Bins in panels (a) and (b) are log spaced to better reflect the data range. ADV = acoustic Doppler velocimeter.

deployment period. In Figure 9, each column shows a different stress component (viscous, turbulent, and wave from left to right), normalized by the total stress τ_T (equation (9)). Each row shows a different set of wave conditions (weak, moderate, and strong from top to bottom). The viscous stress (leftmost column) is strongest close to the bed as expected, though it is generally the weakest component and rarely comprises a significant portion of the total stress. As waves increase in strength (from Figures 9a to 9d to 9g), the viscous stress contribution decreases. This could be due to the dominance of the wave-induced stress (Figure 9i) or wave-current interactions which can weaken velocity gradients by enhancing near-bed momentum mixing (Nielsen, 1992).

The turbulent Reynolds stress (center column) is damped near the bed but is often the dominant stress component by approximately 0.7 cmab in the weak wave case (Figure 9b). The moderate wave case has the most scatter, though in general the turbulent Reynolds stress (Figure 9e) is less dominant than the wave-induced stress (Figure 9f) close to the bed, but comprises an increasing portion of the stress further from the bed. In the strong wave case, the turbulent Reynolds stress (Figure 9h) remains weak relative to the wave-induced stress (Figure 9i) over the entire profile, as the wave-induced stress dominates from 0.5 cmab upward.

Trends in the relative magnitudes of the stress terms in Figures 8 and 9 make sense, but the sign of the wave momentum flux profiles is less intuitive. The expected sign of wave-induced production ($P_w = \overline{\tilde{u}\tilde{w}}\frac{\partial \bar{u}}{\partial z}$) has been examined by previous studies with conflicting results. One set of laboratory experiments showed that $P_w > 0$ over the water column, indicating that energy is transferred from the waves to the mean current (Cheung, 1985; Jiang et al., 1990). Other researchers found $P_w < 0$ in the majority of their experiments, suggesting that the waves were often gaining energy from the mean flow (Thais & Magnaudet, 1996; Reidenbach et al., 2007). We found both situations in our data, as shown in Figure 10.

Figure 10a shows histograms of turbulence production ($P_T = \overline{u'w'}\frac{\partial \bar{u}}{\partial z}$) from the Vectrino profile over 0.4–1.4 cmab. As expected, $P_T < 0$ for nearly the entire deployment at every measurement depth, ensuring a positive turbulence production term in the TKE equation. Conversely, the wave-induced production P_w is both positive and negative (though it is skewed toward negative). In most of the cases shown in Figure 8, we found $\overline{\tilde{u}\tilde{w}} < 0$ regardless of the mean current direction. This is expected from classical theory (Longuet-Higgins, 1953) and indicates that waves tend to pump positive momentum into the near-bed region. Therefore, it is not surprising that Figure 10b shows both positive and negative values of P_w.

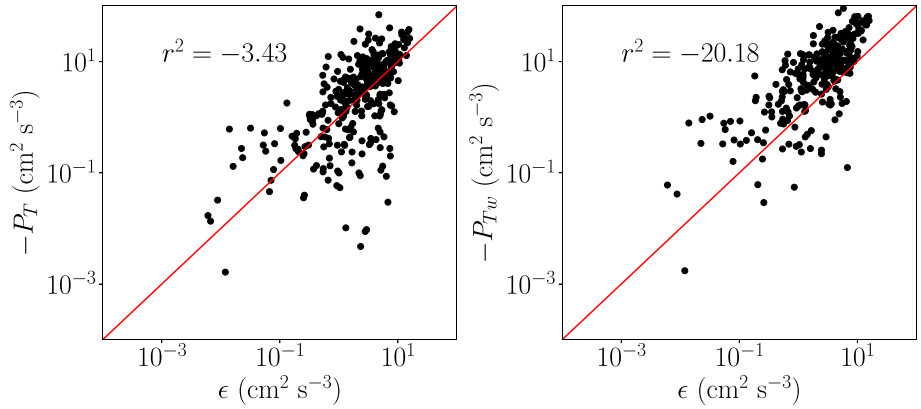

Figure 11. The turbulence kinetic energy dissipation rate, ϵ, plotted against (a) turbulence production and (b) combined wave and turbulence production. All values are calculated from Vectrino data at 0.6 cmab. The red line indicates a one-to-one fit, with the r^2 value indicating the coefficient of determination.

The ADV turbulence production terms, shown in Figure 10c, are also skewed heavily negative and decrease in magnitude with distance from the bed. Unlike the Vectrino data, the ADV wave production terms (Figure 10d) are generally smaller in magnitude than the associated turbulence production, which makes sense because wave production is strongest near the bed. For the majority of measurement bursts, P_w was negative, indicating that the wave field higher in the water column was primarily extracting energy from the mean flow (Thais & Magnaudet, 1996). We also found that most of the positive P_w values in the 15- and 45-cmab ADV data occurred when waves were strong relative to currents, that is, corresponding to the case in Figure 8a. This suggests that when they were strong, the waves were acting as a source of energy to the mean currents, as has been observed in previous laboratory experiments (Jiang et al., 1990).

To elucidate the various energy transfer mechanisms among the waves, turbulence, and mean flow, we attempted to close the combined wave-current TKE budget (Reynolds & Hussain, 1972). While the full transport equation proved difficult to close, we found an approximate balance near the bottom boundary between the TKE dissipation rate, ϵ, and turbulence production,

$$\overline{u'w'}\frac{\partial \overline{u}}{\partial z} + \epsilon = 0. \tag{27}$$

Figure 11a shows ϵ against $-P_T$, while Figure 11b shows ϵ against the combined wave and current production ($-P_{Tw} = -P_T - P_w$), a term that appears in the full wave-current TKE budget. Because Figure 11 is plotted in log-log space, only positive values of $-P_T$ and $-P_{Tw}$ are shown. The coefficient of determination (r^2) values shown in the figure, however, is calculated using all values of dissipation and production regardless of sign. Because they are not based on linear regression, the r^2 values can be negative for the poorer fits. The agreement in Figure 11a is reasonable, indicating that TKE dissipation primarily balances turbulence production. In general, turbulence production is larger than dissipation; given the high concentrations of suspended sediment and resulting density gradients near the bed, it is possible that the buoyancy flux (which we do not account for) serves as an additional sink of TKE.

As shown in Figure 11b, adding the wave production term decreases the correlation with dissipation by increasing the magnitude of the total production term. This indicates that the wave momentum flux is not necessarily balanced by an increase in near-bed dissipation, as has been observed for flows over seagrass canopies (Luhar et al., 2010, 2013). Nonetheless, the wave momentum flux often plays a dominant role in momentum exchange dynamics: the relative magnitudes of $\overline{u'w'}$ and $\overline{\tilde{u}\tilde{w}}$ were consistent throughout the time series, with $\overline{u'w'}$ only dominating $\overline{\tilde{u}\tilde{w}}$ when the wave orbital velocity was approximately an order of magnitude less than the depth-averaged current velocity. This is likely due to the smaller scale of the wave boundary layer compared to the mean current boundary layer. Over the deployment period, the mean viscous sublayer thickness was $5\nu/u_* = 2.0$ mm, while the mean wave boundary layer thickness was $(2\nu/\omega)^{1/2} = 0.9$ mm. This results in sharper gradients and more shear in the wave-induced velocity near the bed. Therefore, for a given velocity magnitude the stress gradients are stronger due to waves than they are due to mean currents. These large wave-induced momentum fluxes near the bed have major implications

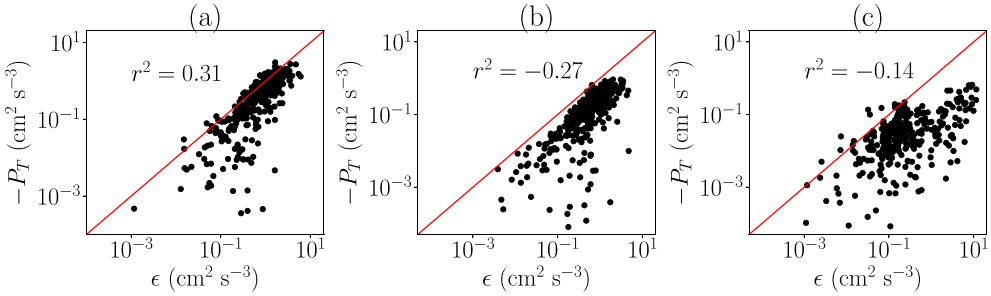

Figure 12. The turbulence kinetic energy dissipation rate, ϵ, plotted against turbulence production measured by acoustic Doppler velocimeters at (a) 5, (b) 15, and (c) 45 cmab. The red line indicates a one-to-one fit, with the r^2 value indicating the coefficient of determination.

for sediment transport because they are more likely to erode the bed. This result is consistent with numerous studies that have emphasized the importance of waves in resuspending cohesive sediments (Brand et al., 2010; Friedrichs et al., 2000; MacVean & Lacy, 2014).

We also applied the TKE balance (equation (27)) to the ADV data at 5, 15, and 45 cmab, as shown in Figure 12. At 5 cmab (Figure 12a) we find a reasonable balance, though dissipation slightly outweighs turbulence production. This disparity grows larger at 15 and 45 cmab, showing that $\epsilon > -P_T$ over most of the water column. Contrasting with the Vectrino data in Figure 11, adding the ADV wave production term increases the correlation to dissipation at each location in the water column (not shown). However, it is difficult to say whether dissipation is elevated as a result of wave production or if turbulence production is suppressed by another mechanism. A previous study conducted in a wavy flow also found that dissipation was larger than the shear production magnitude throughout the water column (Feddersen et al., 2007), suggesting that vertical diffusion of TKE may play an important role in the energy budget. Whitecapping waves have also been shown to enhance TKE dissipation throughout the water column in shallow, wavy flows (Jones & Monismith, 2008). Either of these explanations would be reasonable for our data too.

4.5. Estimation of the Friction Velocity

The analysis conducted so far has already shown how some of the friction velocity estimates in Table 2 will compare to one another. For example, we know that regressing for u_* using the traditional log law (equation (19)) is not appropriate for this system given the canopy flow dynamics. We also saw in Figure 9 that both the viscous stress estimate (equation (14)) and the turbulent stress estimate (equation (24)) rarely make up a significant portion of the total stress near the bed on their own. The combined viscous-turbulent estimate (equation (23)) would show better agreement with the total stress but only during the weak wave cases. Therefore, we are left with three additional friction velocity estimates: u_{*_c} from the Vectrino canopy

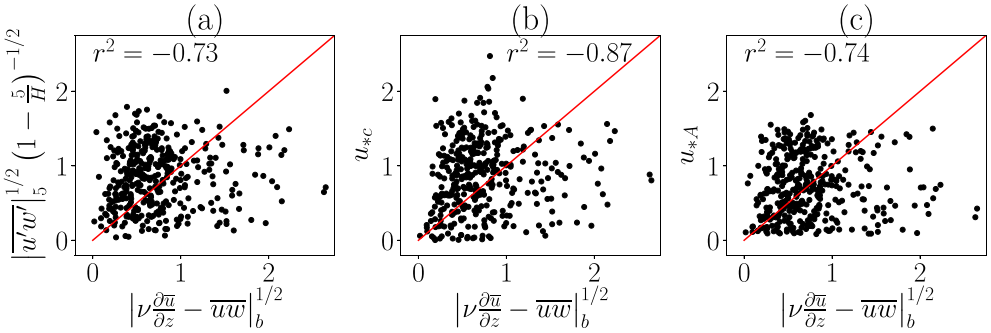

Figure 13. The full bed shear stress $\left|\nu\frac{\partial\overline{u}}{\partial z}-\overline{uw}\right|_b^{1/2}$, calculated with $b = 1$ mm above the canopy top, compared with estimating u_* as (a) $\left|\overline{u'w'}\right|_5^{1/2}\left(1-\frac{5}{H}\right)^{-1/2}$, the turbulent Reynolds stress from the acoustic Doppler velocimeter at 5 cmab extrapolated to the bed, (b) u_{*_c}, the friction velocity estimated from a log law fit (equation (20)) to Vectrino mean velocity data, and (c) u_{*_A} from the acoustic Doppler current profiler mean current profile. All units are in centimeters per second, and the red line indicates a one-to-one fit, with the r^2 value indicating the coefficient of determination.

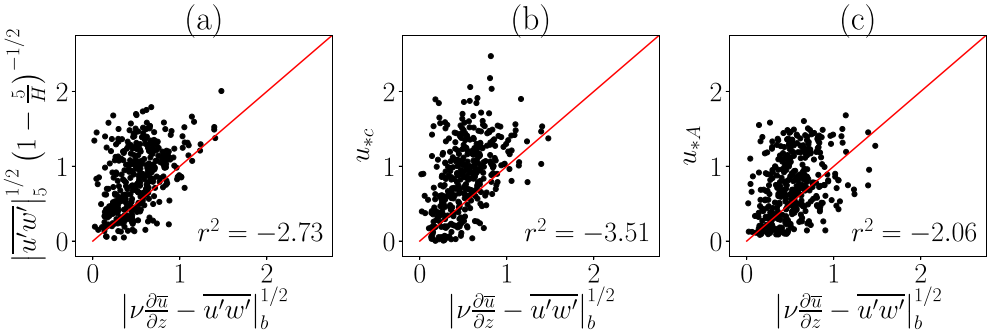

Figure 14. The bed shear stress solely due to currents $\left|\nu\frac{\partial\overline{u}}{\partial z} - \overline{u'w'}\right|_b^{1/2}$, calculated with $b = 1$ mm above the canopy top, compared with estimating u_* as (a) $\left|\overline{u'w'}\right|_5^{1/2}\left(1 - \frac{5}{H}\right)^{-1/2}$, the turbulent Reynolds stress from the acoustic Doppler velocimeter at 5 cmab extrapolated to the bed, (b) u_{*c}, the friction velocity estimated from a log law fit (equation (20)) to Vectrino mean velocity data, and (c) u_{*A} from the acoustic Doppler current profiler mean current profile. All units are in centimeters per second, and the red line indicates a one-to-one fit, with the r^2 value indicating the coefficient of determination.

log law fit (equation (20)), $|\overline{u'w'}|_5^{1/2}\left(1 - \frac{5}{H}\right)^{-1/2}$ from the 5-cmab ADV data (equation (17)), and $u*_A$ from a canopy log law fit to the ADCP mean velocity profile (equation (20)). Each of these estimations is compared to the full bottom stress (equation (22)) in Figure 13, with r^2 values indicating goodness of fit.

None of the methods shown in Figure 13 provide adequate estimations of the bed stress. Most commonly, they overestimate the stress compared to its true value, though there is significant scatter both above and below the one-to-one lines. It is likely that an underestimation of the stress corresponds to a strong wave burst period, as none of the estimation methods explicitly account for wave activity. Conversely, an overestimate of the stress could be attributed to the presence of the bed itself, which acts to reduce velocity and pressure fluctuations (e.g., Hunt & Graham, 1978), thus limiting the stress the bed feels. The same effect could be caused by near-bed sediment-induced stratification as well. None of the estimation methods shown in Figure 13 account for these boundary effects; indeed, the shear stress profile used in deriving the estimation methods assumes that the stress increases linearly toward the boundary, which of course is not true.

Given that the three estimation methods in Figure 13 do not account for waves, a fairer assessment of their validity is found in Figure 14. Here, we compare them to the bed shear stress due solely to currents, that is, the sum of the viscous and turbulent stress components 1 mm above the canopy top (equation (23)). Surprisingly, the goodness of fit decreases substantially in each case compared to the full stress in Figure 13. The scatter is reduced, though, and the errors are primarily overestimates of the bed shear stress. This helps confirm our analysis from Figure 13, suggesting that the more traditional estimates of bed shear stress tend to overestimate the actual current-induced bed shear stress by failing to account for boundary effects. Interestingly though, these estimation methods often do a better job of representing the full bed shear stress because the wave stresses compete against the near-bed viscous damping. Of course, they do not always perform better; during strong wave bursts, they underestimate the bed shear stress substantially.

Overall, none of the estimation methods accurately predict either the full bed shear stress or the current-induced bed shear stress. Even when they perform best, they do so for the wrong reasons: their overestimation of the bed shear stress is merely compensated for by unresolved wave stresses. Further, no measurement outside the boundary layer was able to predict the structure of the mean velocity (and thus the mean bed shear stress) near the bed, because they could not resolve the canopy shear mixing layer dynamics. This discrepancy could lead to significant overestimations of the mean shear at the bed necessary to, for example, initiate sediment motion.

Despite the failure to predict dynamics near the bed, traditional measurements were largely consistent with one another outside the canopy region. Figure 15 shows the canopy log law fit to the Vectrino velocity profile (equation (20)) against the 5-cmab ADV friction velocity estimate (equation (17)) and the ADCP log law estimate (equation (20)). Coefficient of determination values are substantially higher than in Figures 13 and

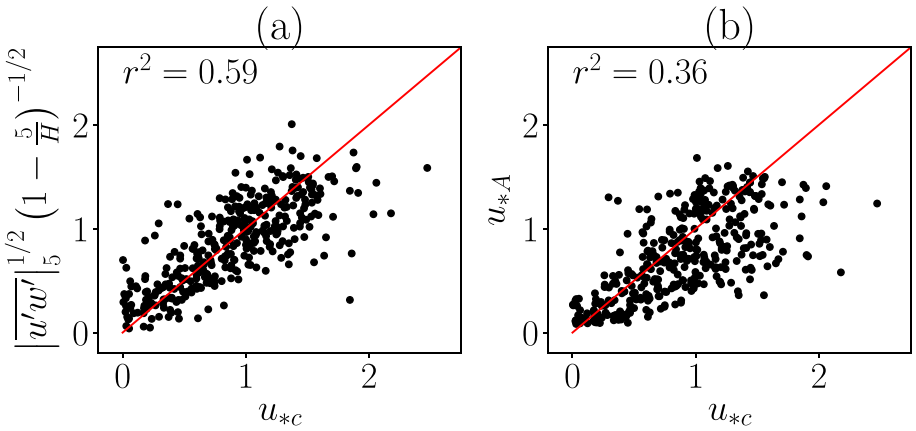

Figure 15. The friction velocity, u_{*c}, estimated from fitting the Vectrino mean velocity profile to the canopy log law (equation (20)) compared to (a) $\left|\overline{u'w'}\right|_5^{1/2}\left(1-\frac{5}{H}\right)^{-1/2}$, the turbulent Reynolds stress from the acoustic Doppler velocimeter at 5 cmab extrapolated to the bed and (b) u_{*A} from the acoustic Doppler current profiler mean current profile. All units are in centimeters per second, and the red line indicates a one-to-one fit, with the r^2 value indicating the coefficient of determination.

14, indicating that the assumption of a logarithmic velocity profile is valid throughout most of the water column. And while these estimates do not accurately predict the total stress measured by the Vectrino at the bed, the Vectrino only sampled at a single location; horizontal variations in bed geometry would lead to corresponding changes in the local bed stress. Log law fitting and turbulence measurements outside the wave boundary layer cannot resolve those variations and therefore provide reasonable estimates of the stress dynamics in the bulk flow.

4.6. Vectrino Error Analysis

Given the novelty of the canopy flow observed and discussed in section 4.2, it is necessary to ensure that the near-zero velocities above the bed and the mixing layer velocity profile are not merely artifacts of the measurement technique. Contrasting with our results, two recent field studies involving a Vectrino deployed with its measurement profile at the sediment-water interface found evidence of a viscous sublayer above a smooth sediment bed (Brand et al., 2016; Wengrove & Foster, 2014). This indicates that the Vectrino is capable of measuring viscous sublayer profiles in situ when the bed is smooth and that our canopy shear mixing layer profiles are likely due to the worm tube canopy rather than artificial thickening of a viscous sublayer. We also conducted a laboratory test to measure wave-induced velocity profiles above a smooth cohesive sediment bed composed of South San Francisco Bay mud. We found that the velocity decayed to zero at the bottom boundary, unlike our field measurements in which the velocity decayed to zero at the top of the canopy. These results mirrored those found in a recent laboratory study using a Vectrino in a sediment flume (Hooshmand et al., 2015). This is further evidence that our reported velocity profiles are showing physical flow features rather than measurement errors.

As discussed in section 3.2, $\overline{\tilde{u}\tilde{w}}$ is assumed to be zero for irrotational, periodic waves. Therefore, it is surprising that it dominates the total momentum flux during wavy conditions. Previous studies have noted that slight tilts in velocimeter orientation or a gently sloping bed can induce erroneously large $\overline{\tilde{u}\tilde{w}}$ measurements (Trowbridge, 1998). On the other hand, given the proximity to the bed, the irrotationality assumption could be violated which would indicate that the values of $\overline{\tilde{u}\tilde{w}}$ are not simply due to measurement error. To check whether or not this is the case, we calculated the quantity

$$\phi = \frac{\overline{\tilde{u}\tilde{w}}}{\sqrt{\overline{\tilde{u}^2}}\sqrt{\overline{\tilde{w}^2}}}. \tag{28}$$

As $|\phi| \to 0$, the phase angle between $\tilde{u}$ and $\tilde{w}$ approaches 90°, and the wave-induced stress becomes negligible. For erroneous measurements, we would expect $\mathcal{O}(10^{-2})$ values of $|\phi|$ (Bricker & Monismith, 2007). As $|\phi| \to 1$, the phase angle approaches 0°, indicating that the wave-induced stress is nonnegligible and induced by physics rather than measurement error. Over the measurement period, the mean value of $|\phi|$ for the Vectrino measurements was $|\phi| = 0.42$, suggesting that $\overline{\tilde{u}\tilde{w}}$ is significant near the bed. For the

ADV data, $|\phi|_5 = 0.17$, $|\phi|_{15} = 0.23$, and $|\phi|_{45} = 0.15$ over the measurement period for the ADVs at 5, 15, and 45 cmab, respectively. This indicates that the near-bed wave-induced vorticity remains nonnegligibly higher in the water column but generally decreases with distance from the bed.

5. Conclusions

We conducted field work with the goal of characterizing the mean and turbulence properties of the wave-current boundary layer in a shallow flow over a cohesive sediment bed. We found that the mean velocity structure in the near-bed region resembled a canopy flow shear mixing layer, rather than a viscous sublayer. This resulted in a decreased mean bed shear stress compared to what one would calculate by fitting a log law to the mean current profile.

We also found that the addition of waves to mean currents increased the net drag felt by the flow. When quantifying bottom drag using a bed shear stress based solely on the currents (i.e., the traditional approach), the drag increased because waves modified the mean velocity profile, leading to an increased apparent bottom roughness. Including the wave momentum flux in the bottom drag calculation also led to an increase in drag, though this followed directly from modification of the bed shear stress by the wave momentum flux.

While these results are qualitatively consistent with numerous wave-current boundary layer models, they also illustrate the inherent limitations and faulty assumptions in those models. Namely, no wave-current boundary layer model that we are aware of directly accounts for the wave momentum flux. Rather, most parameterize the effect of waves through a combined wave-current friction velocity, which itself defines a logarithmic velocity profile inside the wave boundary layer (Grant & Madsen, 1979; Styles et al., 2017; Styles & Glenn, 2000). The velocity profiles that we measured were not logarithmic inside the wave boundary layer, and we found that the wave momentum flux was often the dominant component of the total bed shear stress. This suggests a fundamentally different mechanism for wave-induced increases in bottom drag, and one that we expect is important over any bed rough enough to break the orthogonality between the horizontal and vertical wave velocities.

These results emphasize the importance of detailed bed roughness characterization in combined wave-current flows. In our data, we found relative roughness values of $A/k_b = \mathcal{O}(0.1 - 1)$, a similar magnitude to wave-driven flows over rough coral canopies (Rogers et al., 2016). Therefore, it is not surprising that we see canopy flow dynamics, for example, a strong near-bed wave-induced momentum flux and hyperbolic tangent velocity profile. While many models (e.g., Styles et al., 2017) can be applied to roughness values of $A/k_b < 1$, they will not resolve those canopy flow features, highlighting the need for a wave-current boundary layer model that can be applied over an arbitrarily rough canopy-like bed.

Despite the dominance of the wave momentum flux, TKE dissipation was still reasonably balanced by turbulence production near the bed. This can be partially attributed to the dissipation calculation method, which was based on the high-frequency velocity spectra. Finally, we compared different methods of estimating the friction velocity, u_*, and found that while the estimations were consistent outside the wave boundary layer, the measured shear stress at the bed was not well approximated by any of the estimation techniques, mainly due to unresolved canopy flow dynamics and wave momentum fluxes. These deficiencies could lead to critical errors in sediment transport models, the predictive capabilities of which are determined in large part by whether or not the bed shear stress is accurately estimated. Our measurements indicate that flat plate boundary layer theory can fall short in this regard.

Acknowledgments
G. E. gratefully acknowledges the support of the Charles H. Leavell Graduate Fellowship, and M. C. acknowledges the support of the Stanford Vice Provost for Undergraduate Education. This work was funded by the U.S. National Science Foundation under Grant OCE-1736668. We thank Frank Spada, Kara Scheu, Grace Chang, Craig Jones, Sam McWilliams, Stephen LaMothe, and Jim Christmann for their assistance with the field work. We also thank the two anonymous reviewers whose comments greatly improved the quality of this manuscript. The data used in this paper can be accessed online (http://web.stanford.edu/group/efml-data-repo).

References

Benilov, A. Y., & Filyushkin, B. (1970). Applications of the linear filtration methods to the fluctuation analysis in the sea upper layer. *Izvestiya. Atmospheric and Oceanic Physics, English Translation*, *6*(8), 477–482.

Brand, A., Lacy, J., Hsu, K., Hoover, D., Gladding, S., & Stacey, M. (2010). Wind-enhanced resuspension in the shallow waters of South San Francisco Bay: Mechanisms and potential implications for cohesive sediment transport. *Journal of Geophysical Research*, *115*, C11024. https://doi.org/10.1029/2010JC006172

Brand, A., Noss, C., Dinkel, C., & Holzner, M. (2016). High-resolution measurements of turbulent flow close to the sediment-water interface using a bistatic acoustic profiler. *Journal of atmospheric and oceanic technology*, *33*(4), 769–788.

Bricker, J. D., Inagaki, S., & Monismith, S. G. (2005). Bed drag coefficient variability under wind waves in a tidal estuary. *Journal of Hydraulic Engineering*, *131*(6), 497–508.

Bricker, J. D., & Monismith, S. G. (2007). Spectral wave-turbulence decomposition. *Journal of Atmospheric and Oceanic Technology*, *24*(8), 1479–1487.

Chen, D., Chen, C., Tang, F.-E., Stansby, P., & Li, M. (2007). Boundary layer structure of oscillatory open-channel shallow flows over smooth and rough beds. *Experiments in fluids*, *42*(5), 719–736.
Cheng, R. T., Ling, C.-H., Gartner, J. W., & Wang, P. (1999). Estimates of bottom roughness length and bottom shear stress in South San Francisco Bay, California. *Journal of Geophysical Research*, *104*(C4), 7715–7728.
Cheung, T. K. (1985). A study of the turbulent layer in the water at an air-water interface (Tech. Rep.): STANFORD UNIV CALIF DEPT OF CIVIL ENGINEERING.
Dean, R. G., & Dalrymple, R. A. (1991). *Water wave mechanics for engineers and scientists* (Vol. 2). Hackensack, NJ: World Scientific Publishing Company.
Feddersen, F., Trowbridge, J. H., & Williams III, A. (2007). Vertical structure of dissipation in the nearshore. *Journal of Physical Oceanography*, *37*(7), 1764–1777.
Finnigan, J. (2000). Turbulence in plant canopies. *Annual review of fluid mechanics*, *32*(1), 519–571.
Friedrichs, C., Wright, L., Hepworth, D., & Kim, S. (2000). Bottom-boundary-layer processes associated with fine sediment accumulation in coastal seas and bays. *Continental Shelf Research*, *20*(7), 807–841.
Ghisalberti, M., & Nepf, H. M. (2002). Mixing layers and coherent structures in vegetated aquatic flows. *Journal of Geophysical Research*, *107*(C2), 3011. https://doi.org/10.1029/2001JC000871
Goring, D. G., & Nikora, V. I. (2002). Despiking acoustic doppler velocimeter data. *Journal of Hydraulic Engineering*, *128*(1), 117–126.
Grant, W. D., & Madsen, O. S. (1979). Combined wave and current interaction with a rough bottom. *Journal of Geophysical Research*, *84*, 1797–1808. https://doi.org/10.1029/jc084ic04p01797
Grant, W. D., & Madsen, O. S. (1982). Movable bed roughness in unsteady oscillatory flow. *Journal of Geophysical Research*, *87*, 469–481. https://doi.org/10.1029/jc087ic01p00469
Grant, W. D., & Madsen, O. S. (1986). The continental-shelf bottom boundary layer. *Annual Review of Fluid Mechanics*, *18*(1), 265–305.
Gust, G. (1976). Observations on turbulent-drag reduction in a dilute suspension of clay in sea-water. *Journal of Fluid Mechanics*, *75*(1), 29–47.
Håkanson, L., & Jansson, M. (2002). *Principles of lake sedimentology*. New Jersey: The Blackburn Press.
Hooshmand, A., Horner-Devine, A. R., & Lamb, M. P. (2015). Structure of turbulence and sediment stratification in wave-supported mud layers. *Journal of Geophysical Research: Oceans*, *120*, 2430–2448. https://doi.org/10.1002/2014JC010231
Hunt, J., & Graham, J. (1978). Free-stream turbulence near plane boundaries. *Journal of Fluid Mechanics*, *84*(2), 209–235.
Jensen, B., Sumer, B., & Fredsøe, J (1989). Turbulent oscillatory boundary layers at high Reynolds numbers. *Journal of Fluid Mechanics*, *206*, 265–297.
Jiang, J.-Y., & Street, R. L. (1991). Modulated flows beneath wind-ruffled, mechanically generated water waves. *Journal of Geophysical Research*, *96*, 2711–2721. https://doi.org/10.1029/90JC02259
Jiang, J.-Y., Street, R. L., & Klotz, S. P. (1990). A study of wave-turbulence interaction by use of a nonlinear water wave decomposition technique. *Journal of Geophysical Research*, *95*, 16,037–16,054. https://doi.org/10.1029/jc095ic09p16037
Jones, N. L., & Monismith, S. G. (2008). The influence of whitecapping waves on the vertical structure of turbulence in a shallow estuarine embayment. *Journal of Physical Oceanography*, *38*(7), 1563–1580.
Jonsson, I. G. (1966). Wave boundary layers and friction factors. *Coastal Engineering Proceedings*, *1*(10), 9.
Lacy, J. R., & MacVean, L. J. (2016). Wave attenuation in the shallows of San Francisco Bay. *Coastal Engineering*, *114*, 159–168.
Longuet-Higgins, M. S. (1953). Mass transport in water waves. *Philosophical Transactions of the Royal Society of London. Series A, Mathematical and Physical Sciences*, *245*(903), 535–581.
Luhar, M., Coutu, S., Infantes, E., Fox, S., & Nepf, H. (2010). Wave-induced velocities inside a model seagrass bed. *Journal of Geophysical Research*, *115*, C12005. https://doi.org/10.1029/2010JC006345
Luhar, M., Infantes, E., Orfila, A., Terrados, J., & Nepf, H. M. (2013). Field observations of wave-induced streaming through a submerged seagrass (Posidonia Oceanica) meadow. *Journal of Geophysical Research: Oceans*, *118*, 1955–1968. https://doi.org/10.1002/jgrc.20162
MacVean, L. J., & Lacy, J. (2014). Interactions between waves, sediment, and turbulence on a shallow estuarine mudflat. *Journal of Geophysical Research: Oceans*, *119*, 1534–1553. https://doi.org/10.1002/2013JC009477
Magnaudet, J., & Masbernat, L. (1990). Interaction des vagues de vent avec le courant moyen et la turbulence. *Comptes Rendus. Académie des Sciences*, *311*, 1461–1466.
Mehta, A. J., & Partheniades, E. (1982). Resuspension of deposited cohesive sediment beds. In *Proceedings, 18th Coastal Engineering Conference* (pp. 1569–1588). Cape Town, South Africa.
Nagib, H. M., & Chauhan, K. A. (2008). Variations of Von Kármán coefficient in canonical flows. *Physics of Fluids*, *20*(10), 101518.
Nelson, K., & Fringer, O. (2018). Sediment dynamics in wind wave-dominated shallow-water environments. *Journal of Geophysical Research: Oceans*, *123*, 6996–7015. https://doi.org/10.1029/2018JC013894
Nepf, H. M. (2012). Flow and transport in regions with aquatic vegetation. *Annual Review of Fluid Mechanics*, *44*, 123–142.
Nielsen, P. (1992). *Coastal bottom boundary layers and sediment transport* (Vol. 4). Hackensack, NJ: World Scientific Publishing Company.
Poindexter, C., Rusello, P., & Variano, E. (2011). Acoustic doppler velocimeter-induced acoustic streaming and its implications for measurement. *Experiments in fluids*, *50*(5), 1429–1442.
Prandtl, L. (1925). 7. bericht über untersuchungen zur ausgebildeten turbulenz. *ZAMM-Journal of Applied Mathematics and Mechanics/Zeitschrift für Angewandte Mathematik und Mechanik*, *5*(2), 136–139.
Raupach, M., Finnigan, J., & Brunet, Y. (1996). Coherent eddies and turbulence in vegetation canopies: The mixing-layer analogy, *Boundary-layer meteorology 25th anniversary volume, 1970–1995* (pp. 351–382). Dordrecht: Springer.
Reidenbach, M. A., Koseff, J. R., & Monismith, S. G. (2007). Laboratory experiments of fine-scale mixing and mass transport within a coral canopy. *Physics of Fluids*, *19*(7), 075107.
Reynolds, W., & Hussain, A. (1972). The mechanics of an organized wave in turbulent shear flow. Part 3. Theoretical models and comparisons with experiments. *Journal of Fluid Mechanics*, *54*(2), 263–288.
Rogers, J. S., Monismith, S. G., Koweek, D. A., & Dunbar, R. B. (2016). Wave dynamics of a Pacific atoll with high frictional effects. *Journal of Geophysical Research: Oceans*, *121*, 350–367. https://doi.org/10.1002/2015JC011170
Sanford, L. P. (2008). Modeling a dynamically varying mixed sediment bed with erosion, deposition, bioturbation, consolidation, and armoring. *Computers & Geosciences*, *34*(10), 1263–1283.
Sanford, L. P., & Maa, J. P. (2001). A unified erosion formulation for fine sediments. *Marine Geology*, *179*(1), 9–23.
Schlichting, H., & Gersten, K. (2016). *Boundary-layer theory*. Berlin: Springer.
Stacey, M. T., Monismith, S. G., & Burau, J. R. (1999). Measurements of Reynolds stress profiles in unstratified tidal flow. *Journal of Geophysical Research*, *104*, 10933–10949. https://doi.org/10.1029/1998jc900095

Stacey, M. T., & Ralston, D. K. (2005). The scaling and structure of the estuarine bottom boundary layer. *Journal of Physical Oceanography*, *35*(1), 55–71.

Styles, R., & Glenn, S. M. (2000). Modeling stratified wave and current bottom boundary layers on the continental shelf. *Journal of Geophysical Research*, *105*, 24119–24139. https://doi.org/10.1029/2000jc900115

Styles, R., Glenn, S. M., & Brown, M. E. (2017). An optimized combined wave and current bottom boundary layer model for arbitrary bed roughness (*Tech. Rep.*): US Army Engineer Research and Development Center, Coastal and Hydraulics Laboratory Vicksburg United States.

Thais, L., & Magnaudet, J. (1995). A triple decomposition of the fluctuating motion below laboratory wind water waves. *Journal of Geophysical Research*, *100*, 741–755. https://doi.org/10.1029/94jc02714

Thais, L., & Magnaudet, J. (1996). Turbulent structure beneath surface gravity waves sheared by the wind. *Journal of Fluid Mechanics*, *328*, 313–344.

Thomas, R., Schindfessel, L., McLelland, S., Creëlle, S., & De Mulder, T. (2017). Bias in mean velocities and noise in variances and covariances measured using a multistatic acoustic profiler: The Nortek Vectrino Profiler. *Measurement Science and Technology*, *28*(7), 075302.

Trowbridge, J. (1998). On a technique for measurement of turbulent shear stress in the presence of surface waves. *Journal of Atmospheric and Oceanic Technology*, *15*(1), 290–298.

Welch, P. (1967). The use of fast fourier transform for the estimation of power spectra: A method based on time averaging over short, modified periodograms. *IEEE Transactions on Audio and Electroacoustics*, *15*(2), 70–73.

Wengrove, M., & Foster, D. (2014). Field evidence of the viscous sublayer in a tidally forced developing boundary layer. *Geophysical Research Letters*, *41*, 5084–5090. https://doi.org/10.1002/2014gl060709

You, Z.-J., Wilkinson, D., & Nielsen, P. (1991). Velocity distributions of waves and currents in the combined flow. *Coastal Engineering*, *15*(5-6), 525–543.